Investigating the temperature dependent deformation mechanisms of CVD deposited single crystalline TiN films

Project report

Daniel Rainer

Chair of Functional Materials and Materials Systems

Montanuniversität Leoben

Supervisor at home institution: Prof. Christian Mitterer

Supervisor at host institution: Prof. Peter Hosemann

Leoben, July 2023

Project summary

TiN-based thin films are often exposed to mechanical loads at both, room temperature and elevated temperatures. This makes a fundamental understanding of the deformation mechanisms and the influence of stress at elevated temperatures inevitable. In-situ pillar compression tests are frequently carried out to investigate the deformation mechanisms at uniaxial stress whilst observing the deformation using the scanning electron microscope. This technique can be used to examine the deformation behavior of TiN at room and elevated temperatures to gain deeper understanding of the deformation mechanisms.

The aim of this work is to analyze the sample preparation and subsequently the deformation behavior of single crystalline CVD TiN orientated along [100], [110] and [111] at elevated temperatures. Therefore, CVD and fs-laser ablation was carried out to fabricate geometrically suitable samples. EBSD was performed to verify the crystallographic orientation of the indented pillar axes. Pillar preparation was carried out by FIB using a 45° cutting angle approach. First in-situ pillar compression tests at 700 °C for pillars orientated along the crystallographic direction [100] were conducted.

The CVD TiN films show poor layer adhesion for higher deposition pressures than 160 mbar and higher deposition times than 11 h. Processing by fs-laser ablation may result in severe failure of the sample if the dimensions get smaller than 2 mm. Pillar preparation by FIB cutting with a cutting angle of 45° reveal well-shaped pillars with square cross-section and the desired geometry down to 300 nm. First in-situ pillar compression tests of pillars orientated along [100] show size effects and load drops which might indicate plastic deformation. Further experiments could not be carried out due to failure of the sample heater and a different geometry of the new heater. The collaboration on this project between the Department of Materials Science Leoben and the Department of Nuclear Engineering in Berkeley will be continued when the indenter stage is modified.

Content

1. Introduction

Thin films are frequently deposited to improve the surface properties of bulk materials [26]. Especially TiN-based thin films are used in various applications due to their excellent chemical and physical properties [1]. TiN was already used in the 1970's as protective coating of tools against wear and corrosion due to its high hardness and chemical resistance [2]. Nowadays, TiN is the basis for various thin film systems and is utilized for example as diffusion barrier in microelectronics or, owing to its characteristic golden color as decorative coating [2–5]. Used in these fields of application, TiN is frequently exposed to mechanical loads at ambient as well as elevated temperatures. Therefore, testing at or very close to the service temperature of TiN films is indispensable [6].

During the past decades, micromechanical experiments and their unique in-situ and high temperature possibilities established testing of sample volumes at the micro- as well as nanoscale which resulted in deep understanding of the deformation mechanisms of various materials. In-situ pillar compression tests are commonly performed to investigate sample deformation caused by uniaxial stress [7,8]. The uniaxial stresses enable calculations of material plasticity parameters such as the critical resolved shear stress (CRSS) at various temperatures of the material. Micro-cantilever bending tests revealed brittle behavior of single crystalline TiN fracturing after solely elastic deformation [9]. Nanoindentation experiments and DFT calculations showed however, that TiN might show plastic deformation at elevated temperatures [6,10–12]. There are no results of uniaxial testing of TiN at elevated temperatures reported in literature to the best of our knowledge.

The aim of this research project is to learn the sample preparation and to understand the fundamental mechanisms of plastic deformation of single crystalline (sc) TiN thin films orientated along the main crystallographic directions [100], [110] and [111] at elevated temperatures. Therefore, chemical vapor deposition (CVD) of single crystalline TiN onto Al_2O_3 was carried out. Furthermore, femtosecond-laser (fs-laser) processing was performed to receive a suitable geometry to mount the sample for the in-situ pillar compression tests. Electron backscatter diffraction (EBSD) was conducted to confirm the crystallographic orientation of the indented pillar axis. Focused ion beam (FIB) pillar fabrication was carried out at a 45° cutting angle. Finally, first in-situ pillar compression tests were performed along [100] for two different pillar sizes.

2. Theoretical background

2.1. Titanium nitride

TiN is an interstitial metal nitride with a fcc crystal structure (NaCl-type, space group 225 [13]), 8 atoms per unit cell and a lattice parameter of 0.424 nm. It has a high melting point (2950 °C), high hardness, high wear resistance and high chemical resistance at room temperature. The chemical resistance however, decreases with increasing temperature and above 800 °C, it tends to severely oxidize [4]. Due to its versatility, TiN is frequently used as the basis of thin film systems such as TiAlN, TiSiN and TiCN. These TiN-based systems are used for various applications such as diffusion barriers in microelectronics, wear-resistant layers in tooling industry or due to the characteristic golden yellow color, as decorative coatings [4,5,14]. In general, TiN is a brittle material revealing fracture after solely elastic deformation at room temperature [15]. At elevated temperatures however, plastic deformation was observed during nanoindentation experiments [6,11]. The three main slip systems of TiN are $a_0/2\langle 110\rangle\{100\}$, $a_0/2\langle 110\rangle\{110\}$ and $a_0/2\langle 110\rangle\{111\}$ with a_0 being the lattice parameter. Density functional theory calculations revealed a Peierl stress for an edge dislocation of 1.3-1.4 GPa, 2.7-3.2 GPa and 8.7-9.6 GPa for the {110}, {111} and {100} slip planes, respectively. In case of a screw dislocation, the calculated Peierl stresses are 0.4-0.7 GPa for the {110}, 9.0-9.5 GPa for the {111} and more than 15.3 GPa for the {100} slip plane [12]. Taking the calculated Peierl stresses into account, TiN might also plastically deform during in-situ pillar compression tests at elevated temperatures if the pillar width is small enough. Therefore, this will be investigated in this joint project between the University of Leoben and the University of California, Berkeley.

2.2. Chemical vapor deposition

CVD, schematically shown in figure 1 [16] is frequently used to deposit thin films on various base materials, so-called substrates. The latter is placed within a furnace which can heat up to a few hundred or even above 1000 °C. Prior to the CVD process, a catalyst might be deposited onto the substrate to reduce the activation energy and hence the required temperature of the thin film deposition (so-called catalyst-enhanced CVD). After heating up, the precursor gas inlet is opened and the precursor gas flows into the chamber. The selected precursor gas determines the material's composition and decisively influences the characteristics. Frequently used precursors are metal

hydrides, halides, alkyls and carbonyls. Due to the high temperatures during CVD, decomposition, diffusion and chemical reactions of the precursor gas and the substrate surface occur resulting in nucleation and layer growth.

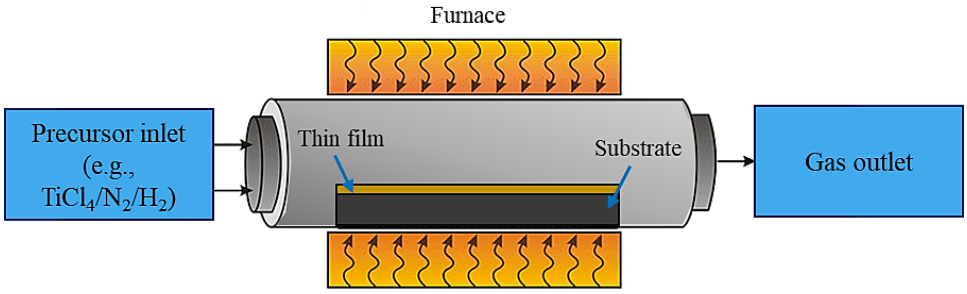

Figure 1: Schematic illustration of the CVD process, adapted from [16].

There are many different types of CVD which can be distinguished by the involved chemical reactions or driving forces and some examples are shortly described.

- Thermally activated CVD: The high temperatures are the driving force for the chemical reactions at the substrate surface. This approach is suitable for substrates which can withstand rather high temperatures.
- Plasma-enhanced CVD: A plasma discharge is initiated to enhance the reactivity of the precursor gases enabling deposition at lower temperatures. This method is applied to deposit thin films on temperature sensitive substrates.
- Flame assisted CVD: The precursors are added to the burning gas of an open flame which is used to heat up the substrate at atmospheric pressures. This method is mainly used for oxides.

The properties of the deposited thin films such as the thickness, composition and morphology can be finely tuned by controlling the process parameters such as the chamber pressure, temperature, precursor flow rate or deposition time. The advantages of CVD are the high accessible deposition rate of even complex-shaped substrates and the precise thickness control. Nevertheless, many precursor gases need careful handling due to flammability, explosivity or toxicity. Exemplary fields of application are the tooling or the semiconductor industry [17].

2.3. Femtosecond-laser ablation

Fs-laser ablation (figure 2 [18]) is utilized to precisely remove material from a target surface using ultra-short laser pulses with a duration of a few fs. These ultra-short pulses are generated by mode locking where an electro-optic modulator enforces a fixed phase relationship and interference of the laser eigenmodes by an electric field [19]. The laser beam is focused on the sample surface by a reflecting mirror and a focus lens. During fs-laser ablation, multiphoton absorption occurs leading to the excitation of electrons from the valence to the conduction band and further to the ablation of the material. The diffusion time of heat from electrons to the lattice atoms is usually in the range of picoseconds and thus the fs-laser ablation results in minimized heat affected zones if the parameters are optimized. Furthermore, even transparent materials can be processed due to the multiphoton absorption which allows to process materials with higher band gap as the average photon energy. An inlet pipe for cutting gas can be implemented in the system to blow away the ablated material during processing. Fs-laser ablation enables processing of various materials with minimized heat affected zones and high precision. Therefore, this technique is frequently used for the fabrication of micro-structured materials such as microchannels or for substrate processing in the semiconductor industry [18].

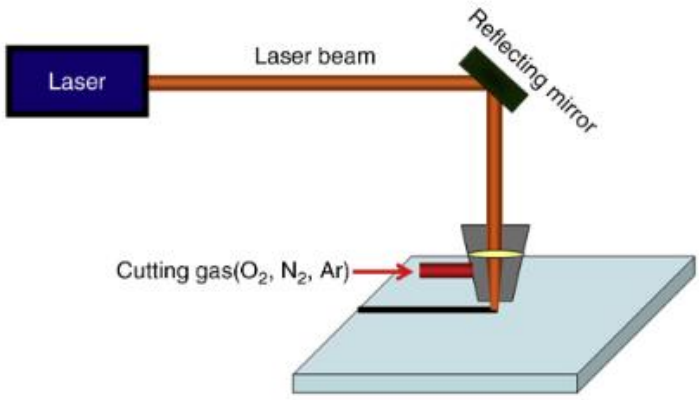

Figure 2: Schematic illustration of a fs-laser system, taken from [18].

2.4. Ion milling

Ion milling (figure 3 [20]) can be used to metallographically prepare samples for further characterization such as scanning electron microscope (SEM) imaging or EBSD without mechanically distorting the surface or damaging internal structures. During ion milling, the sample surface is bombarded with ions (usually Ar^+) which causes material ablation. There are two main approaches frequently used for sample preparation, namely flat milling (figure 3a) and cross-

section milling (figure 3b). Flat milling is utilized after mechanical grinding and polishing to flatten the sample surface with an beam incident angle of almost 90° to the flattened surface. The ion beam reveals the shape of a gaussian curve with the highest intensity in the center of the beam. To prepare the entire sample surface equally, the sample is rotated whereas the ion beam is eucentric to the rotation axis of the sample. Ion cross-section milling can be used without mechanical grinding or polishing prior to the ion milling. A mask is fixated onto the sample and the ion beam mills the protruding material. Contrary to flat milling, the polished surface is parallel to the incident beam. Another advantage of Ion milling is that there is no anisotropic etching as for chemical techniques and thus it might be used for various types of materials such as metals, ceramics and minerals [20,21].

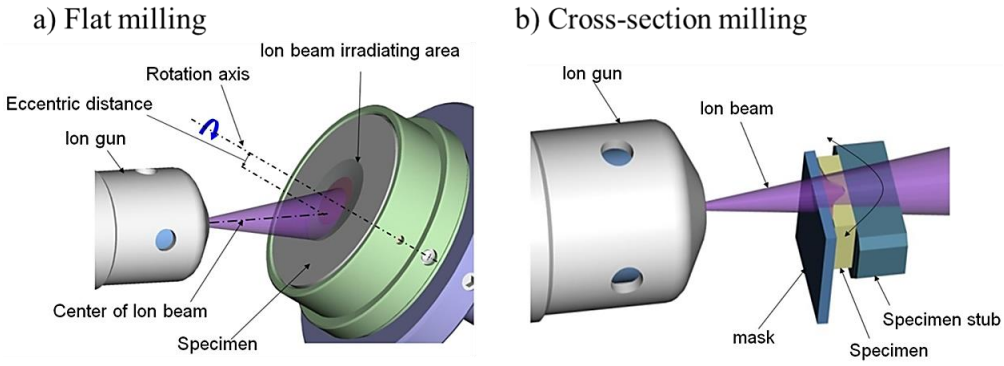

Figure 3: a) flat and b) cross-section ion milling, taken from [20].

2.5. Scanning electron microscope

The scanning electron microscope is widely used to analyze materials at the (sub-) micrometer scale. Developed in the 1930s, the SEM was significantly improved during the past 90 years. The imaging of the SEM is based on interactions of the incident electron beam and the sample surface. The electron-sample interaction results in various signals such as secondary electrons, backscattered electrons, and characteristic X-rays which can be detected. The secondary electrons provide mainly topographical contrast, the backscattered electrons orientational as well as chemical and the X-rays solely chemical information. The detected signal can then be used to create highly detailed images and to obtain information about the chemical composition, morphology, and

topography. Figure 4 [22] shows a schematic illustration of the SEM. The electron gun emits the electrons either by heating a tungsten filament or by field emission caused by a high electric field. Magnetic lenses and apertures control the intensity and focus the electron beam onto the sample surface. The backscattered electron and the secondary electron detector detect the respective electrons. Non-conductive materials can also be investigated if the sample is coated with a conductive layer such as gold. Nevertheless, it is important that the sample is compatible with high vacuum within the SEM chamber and does not evaporate. The SEM is for example utilized to study the microstructure of materials or to examine fracture mechanism. Furthermore, the SEM can be equipped with energy-dispersive X-ray spectroscopy or EBSD detectors to investigate chemical composition and crystallography [22,23]. As EBSD was also used in this work, this technique will be further explained in the next section.

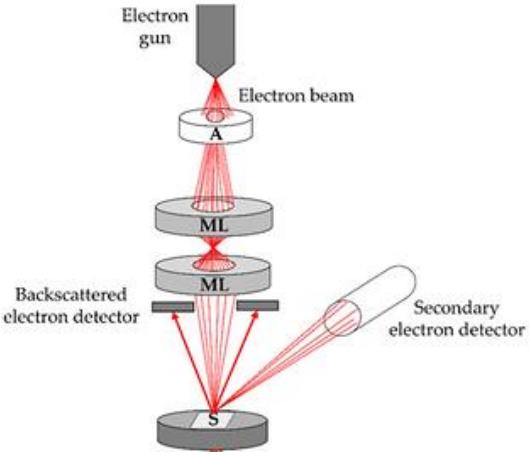

Figure 4: Schematic illustration of the SEM, taken from [22]. ML are magnetic lenses; A is the aperture and S is the sample.

2.6. Electron backscatter diffraction

EBSD (Schematically shown in figure 5a [24]) is a characterization technique widely used to gather crystallographic and microstructural information of a small sample volume with the SEM and an EBSD detector system. The latter consists of a phosphor screen coupled to a photon-sensitive charge coupled device (CCD) camera. To conduct the EBSD measurements, the sample within the SEM is usually tilted 70° to the phosphor screen. The incident electron beam is elastically scattered and diffracted at the individual lattice planes leading to so-called Kossel diffraction cones which intersect with the phosphor screen. The crystal orientation can be determined by Hough

transformation and comparing the data with an internal database. This procedure is then repeated point-by-point within a region of interest and the result might be illustrated using dedicated software such as the EDAX Orientation Imaging Microscopy [25,26]. An exemplary inverse pole figure (IPF) color map of an EBSD measurement of pure copper can be seen in figure 5b [27]. The colors of the individual grains indicate the crystallographic orientation associated with the color legend at the bottom right.

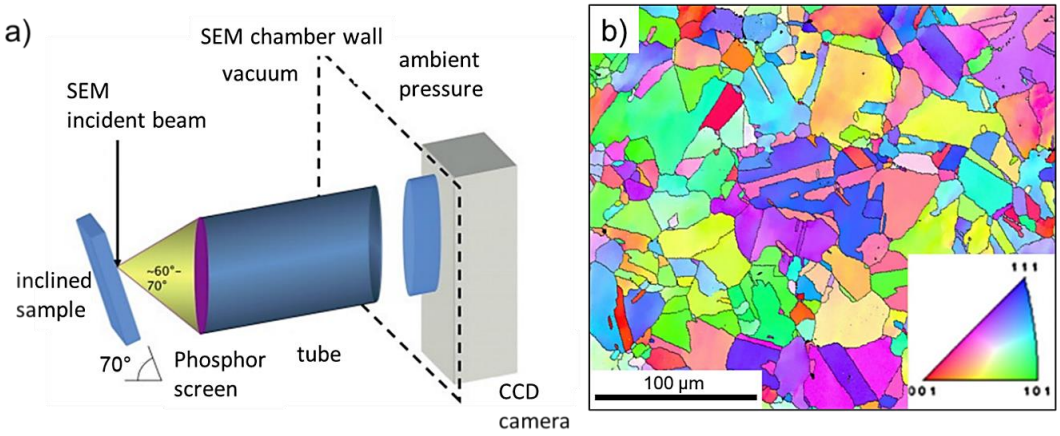

Figure 5: a) Schematic principle of EBSD, taken from [24] and b) exemplary IPF color map of pure copper, taken from [27].

2.7. Focused ion beam system

The FIB system can be used for imaging and micro-/nanofabrication of a wide range of devices or samples. Nowadays, the FIB is frequently combined with an SEM within a dualbeam workstation. The reason for that is the induced contamination and sample damage by FIB imaging due to the impact of the heavy ions. The combination allows precise FIB processing of materials at the nanoscale and gathering information about the surface morphology with minimized damage using the

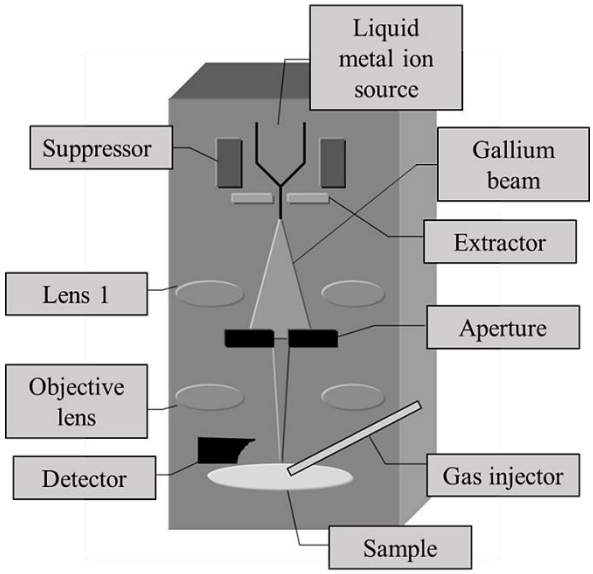

Figure 6: Schematic illustration of the FIB system,, taken from [28]

SEM. Figure 6 [28] shows a schematic illustration of a FIB system. The FIB is usually operated using Ga^+ ions emitted by field emission of a liquid metal ion source. This Ga^+ beam is then accelerated towards the sample surface by an electric field and focused by the magnetic lenses and apertures. The ion beam is either elastically scattered causing material ablation or inelastically scattered which produces secondary electrons, ions and X-rays. The secondary electrons can then be detected by the secondary electron detector of the SEM and used to image the sample surface. Nevertheless, there is always elastic scattering to some extend causing surface damage. Furthermore, the ion beam can also be used to deposit protective layers such as Pt via the gas injector. The FIB is used for example to fabricate TEM lamellas or APT samples for subsequent characterization [28,29]. A further application is preparation of microcantilever or pillars for in-situ pillar compression tests and the latter will be discussed in the next section.

2.8. In-situ pillar compression tests

The miniaturization trend during the past decade, mainly driven by the microelectronic industry made it necessary to understand the mechanical properties and deformation mechanisms at small scales. In-situ pillar compression tests, as shown in figure 7a [30] are commonly used to investigate sample deformation caused by uniaxial stress. Due to the in-situ possibility, deformation can be observed in real-time and correlated with the stress-strain data to get insights in strain hardening and dislocation dynamics. The samples are usually fabricated by subtractive methods like electro-chemical etching, ion milling or FIB processing [31,32]. In-situ pillar compression tests are carried out using a nanoindenter equipped with an appropriate indentation tip such as the flat punch or the berkovich tip for pillar splitting experiments [7]. Challenges are for

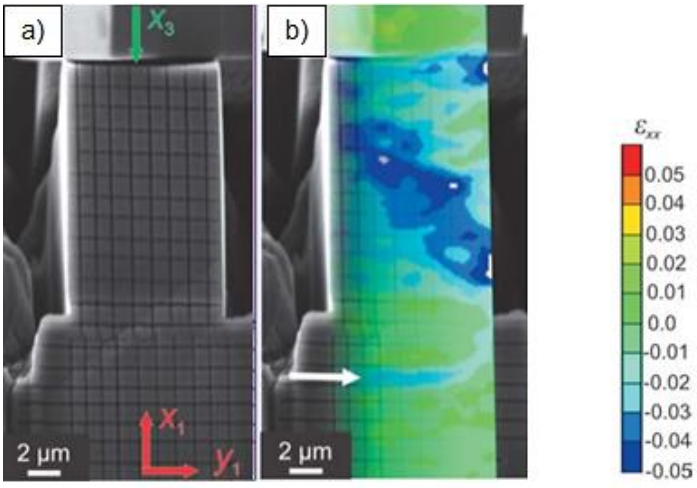

Figure 7: In-situ pillar compression test with a flat punch indentation tip, taken from [30]: a) Micrograph of the experiment, b) Digital image correlation, the white arrow indicates the deformation of the material beneath the pillar.

example the limited sample length to width ratio (aspect ratio) to avoid elastic instability and further buckling of the pillar [33]. Furthermore, it is necessary to ensure that the pillar taper is as small as possible to avoid misinterpretation of stress and strain data. FIB damage, such as ion implantation and the formation of stacking fault tetrahedrons or point defects, might influence the deformation behavior of the sample. Alignment is crucial as misalignment leads to a complex stress state and thus to erroneous results. Another source of error is the sample sink in, which occurs because the base beneath the micropillar is usually the same material as the pillar itself [7,30]. The latter effect can be shown by digital image correlation of the in-situ SEM images during pillar testing (figure 7b [30]). Despite the challenges, in-situ pillar compression testing can be used to gather valuable insights into the deformation behavior of materials at the micro- or nanoscale. Figure 8 [34] shows for example results for pure single crystalline Ni with varying pillar widths and constant aspect ratios. It is evident, that the strength and plasticity is enhanced by decreasing the pillar width. Furthermore, the deformation changes from smooth plastic flow of the bulk material to intermittent and stochastic behavior for micropillars. The results show that the mechanisms of bulk plastic deformation cannot be directly applied for deformation at the micro- or even nanoscale and must be evaluated at the respective scale.

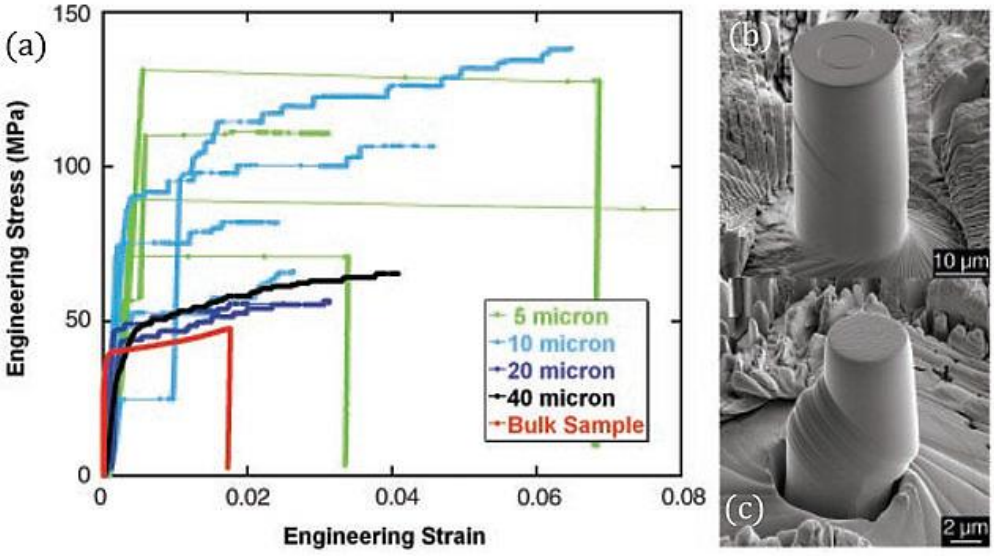

Figure 8: Results of the in-situ pillar compression tests of pure single crystalline Ni, taken from [34]: a) Stress-strain curves for pillars with varying pillar widths and constant aspect ratios. Furthermore, SEM micrographs taken after testing of pillars with a width of b) 20 µm and c) 5 µm.

Using the SEM images and stress-strain data, the shear stress acting on the individual slip system can be calculated. Therefore, the underlying deformation mechanism at the atomic scale can be examined. Schmid's law [35] is used to calculate the shear stress which is defined as

$$\tau = m\sigma \tag{1}$$

with the Schmid factor m (geometrical factor) and the uniaxial compression stress σ acting on the pillar. Figure 9 [36] shows a geometrical illustration of the deviation of Schmid's law which is the result of geometrical considerations. First, the area of the sample cross-section must be converted into the area of the slip plane along the slip direction by the angle between the compression axis and the slip plane normal. Furthermore, the compression force must be converted into the force parallel to the slip direction which is done by using the angle between the slip direction and the compression axis. The Schmid factor *m* is then defined as the multiplication of the two cosinus terms and thus the shown equation in figure 9 is equal to equation (1).

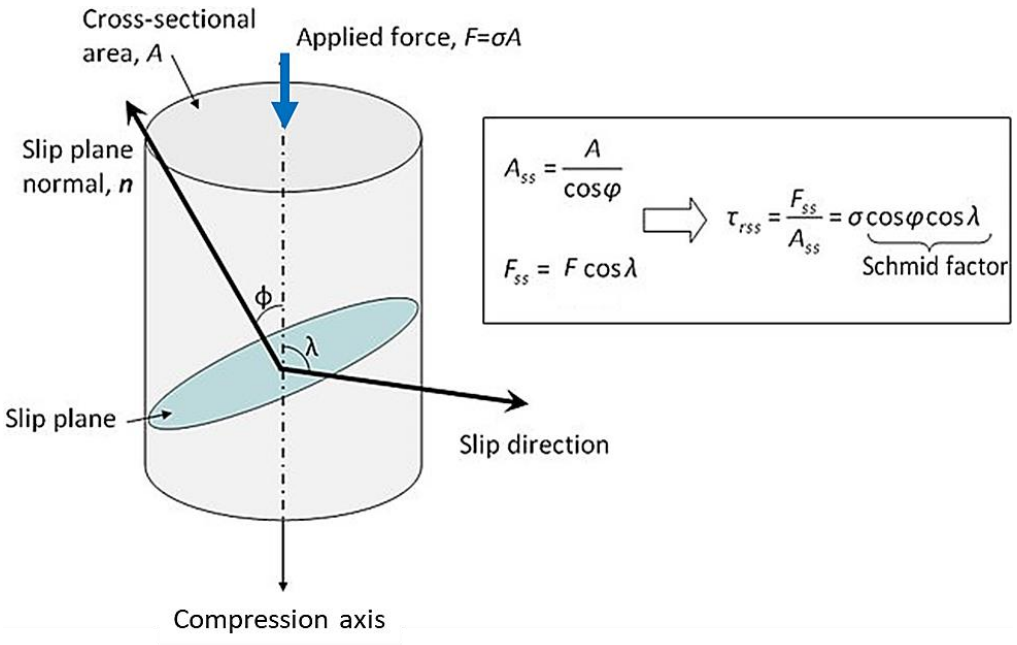

Figure 9: Deviation of Schmid's law, adapted from [36].

3. Methodology

3.1. Chemical vapor deposition

Single crystalline, (110) orientated TiN layers were epitaxially deposited onto $(1\bar{1}01)$ Al_2O_3 substrates using an industrial scale Sucotec SCT600 TH CVD plant. As precursors, a gas mixture of $TiCl_4/N_2/H_2$ was utilized. For a first sample batch, the deposition was carried out for 16 h at a gas pressure of 800 mbar and a temperature of 920 °C to receive a layer thickness of 8 µm. A second batch was deposited at 160 mbar and 920 °C for 11 h to receive a layer thickness of 6 µm. For the second batch, energy dispersive X-ray spectroscopy was performed to analyze the elemental composition. The analysis yielded an elemental composition of 48.9 ± 0.2% Ti and 51.1 ± 0.2% N and thus the TiN layer can be considered stochiometric.

3.2. Femtoscecond-laser ablation

T-shaped samples were cut out of the TiN layer deposited onto the Al_2O_3 substrate to fit in the sample holder of the Hysitron PI88 SEM picoindenter. The latter was performed utilizing a microPREP PRO fs-laser ablation system by 3D Micromac AG. Further fs-laser processing was carried out using a Spectra-Physics Spirit one fs-laser ablation system. In figure 10, a schematic illustration of the cutting procedure of the T-shaped samples is shown. Each red border in figure 10a-c represents a sample after laser cutting with the respective crystallographic orientation of the face perpendicular to the black arrow. Furthermore, the black arrows also indicate the intended pillar axes of the micropillars. The cutting angles to receive the desired orientations are predetermined by the cubic crystal structure of the TiN layer. It has to be noted that the crystal orientation of the substrate differs from the orientation of the TiN layer due to the hexagonal crystal structure of the Al_2O_3 substrate. In the further sections of this report, the T-shaped TiN samples in figure 10a, b and c are referred to as TiN100, TiN110 and TiN111, respectively.

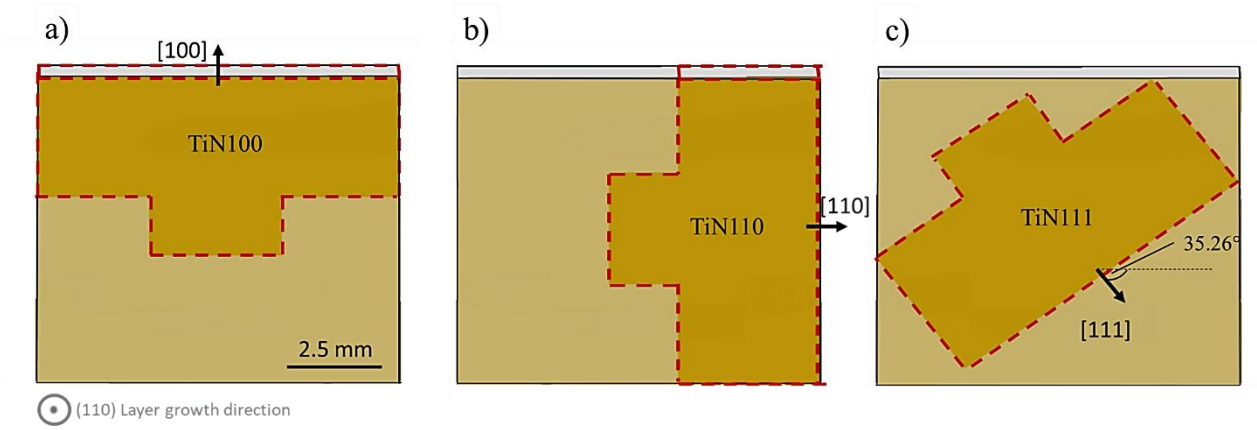

Figure 10: Fs-laser preparation of the T-shaped samples with the respective crystallographic orientation: Schematics of the a) TiN100, b) TiN110 and c) TiN111 preparation. The black arrow indicates the intended pillar axes.

3.3. Ion milling

The faces perpendicular to the black arrows in figure 10 were further prepared to flatten the surface and thus to facilitate the EBSD measurements and the pillar fabrication. To do so, cross-section ion milling with Ar^+ ions was conducted utilizing a Hitachi ArBlade 5000.

3.4. Electron backscatter diffraction

EBSD was carried out to to confirm the crystallographic orientations of the ion milled surfaces and the desired pillar orientations. To do so, a Zeiss DualBeam AURIGA-CrossBeam workstation, equipped with an EDAX Hikari Super EBSD system was used.

3.5. Pillar fabrication

Pillars were fabricated using a Thermo Scientific Scios 2 DualBeam (SEM-FIB) as well as a FEI Quanta 3D DualBeam (SEM-FIB) workstation. The preparation steps are shown in figure 11. Trenches were milled by FIB at 30 kV acceleration voltage and 15 nA beam current (figure 11a-d). In figure 11a, the top-down trenching is shown which was conducted parallel to the growth

direction of the TiN layer and Figure 11b reveals the corresponding SEM image after trenching. Figure 11c shows the front-trenching procedure normal to the growth direction (parallel to the interface) and figure 11d reveals the corresponding SEM image. Pillar coarse cutting was carried out at a cutting angle of 45° at 30 kV acceleration voltage and 1 nA beam current (figure 11e, f). The subsequent fine cutting (figure 11h, i) was performed at 30 kV and 10 pA. Furthermore, the pillars were shortened at a cutting angle of 90° including a coarse (30 kV and 1 nA) as well as a fine cutting step (30 kV and 10 pA) shown in figure 11i. In figure 11j, an exemplary final pillar after all preparation steps is depicted.

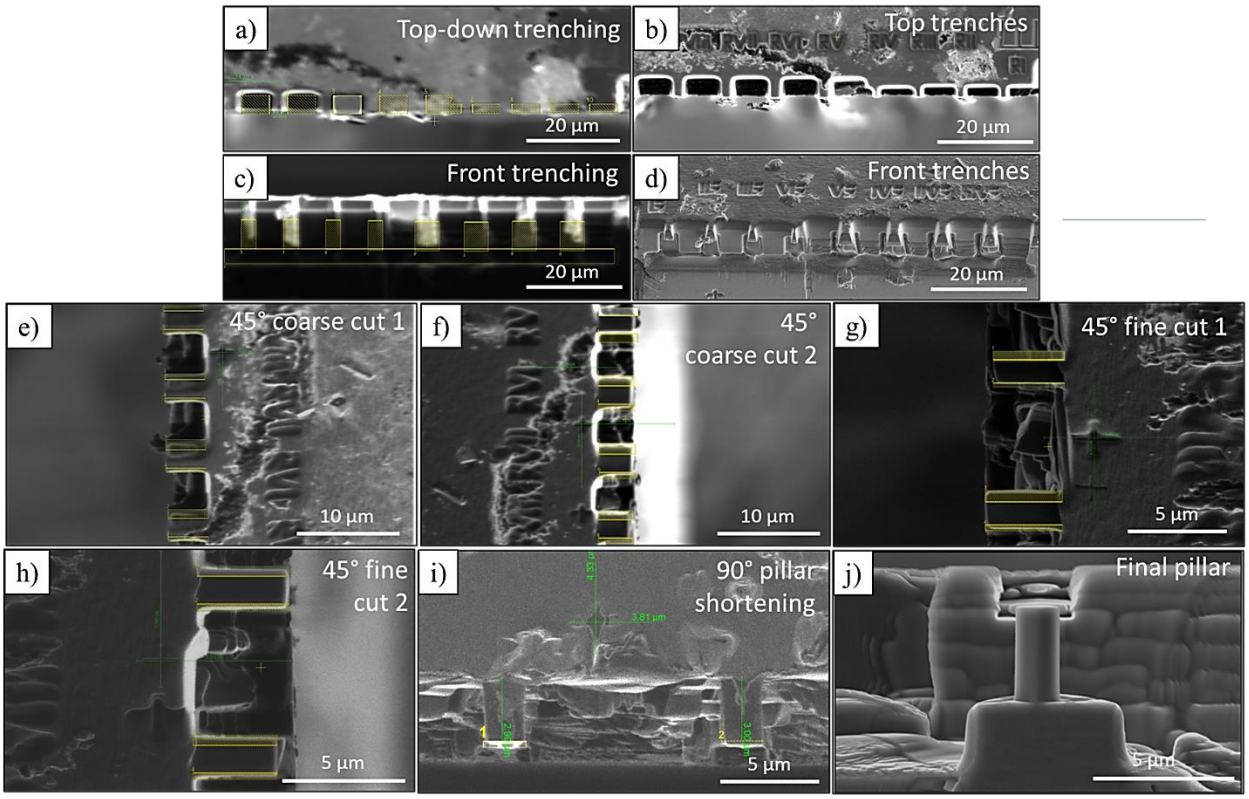

Figure 11: Pillar preparation steps by FIB: a) FIB image of trenching from top, b) SEM image of the top trenches, c) FIB image of the trenching from front, d) SEM image of the final trenches. Furthermore, FIB images of the e) coarse cutting with a cutting angle of 45° from one side and f) from the other, g) pillar shortening, h) fine cutting with a cutting angle of 45° from one side and i) from the other and j) an exemplary final pillar.

Figure 12 illustrates the measurement of the length (figure 12a) and the edge widths of the pillars to calculate the relevant quantities for the data evaluation of the in-situ pillar compression tests.

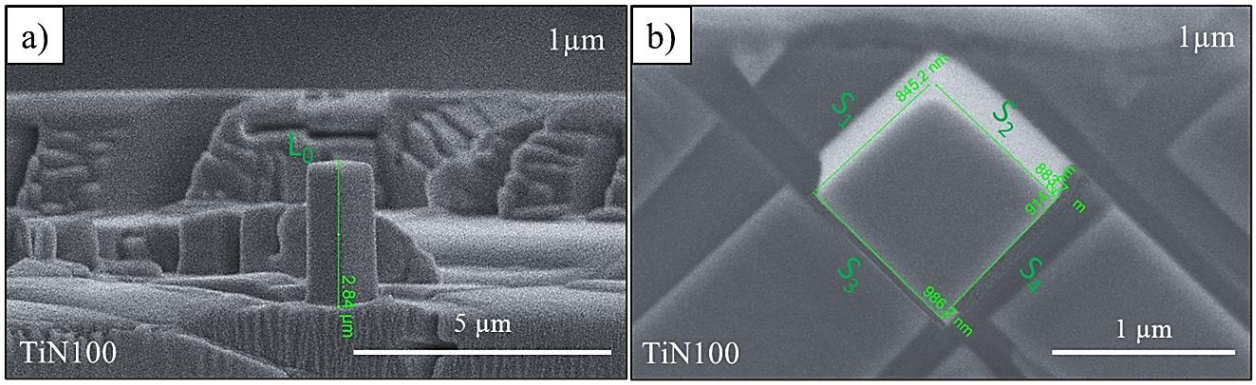

Figure 12: Measuring the a) length and b) widths of the fabricated pillar.

The cross-sectional area was calculated by averaging the measured edge widths and the standard equation for a square

$$A = \left(\frac{(S_1 + S_2 + S_3 + S_4)}{4}\right)^2 \tag{2}$$

with the edge widths S_1, S_2, S_3 and S_4. The aspect ratio AR was calculated by

$$AR = \left(\frac{(S_1 + S_2 + S_3 + S_4)}{4} \cdot \frac{1}{L_0}\right)^{-1} \tag{3}$$

with the initial pillar length L_0. The load and the displacement data were then used to calculate the engineering stress σ and the engineering strain ε by

$$\sigma = \frac{F}{A} \tag{4}$$

$$\epsilon = \frac{\Delta L}{L_0} \tag{5}$$

with the load on the indenter F, the area A, the compression distance ΔL and the initial pillar length L_0. The shear stresses acting on the individual slip systems were calculated using Schmid's law

$$\tau = m\sigma \tag{6}$$

with the Schmid factor *m* and the acting compression stress σ. Furthermore, the Schmid factors of the slip systems of TiN100, TiN110 and TiN111 were calculated after figure 9 and are shown in table 1.

Table 1: Schmid factors of the TiN slip systems for TiN100, TiN110 and TiN111

	TiN100	**TiN110**	**TiN111**
⟨110⟩{100}	0	0.35	0.47
⟨110⟩{110}	0.5	0	0
⟨110⟩{111}	0.41	0	0.27

3.5.1. Pillar geometry study in case of TiN100

To determine a suitable pillar width, three sets of three pillars were fabricated onto the TiN100 sample according to the in section 3.5 described method. Each pillar set had a square cross-section and constant height to width ratio (so-called aspect ratio) of 3 but varying widths of 1 µm (A-set), 600 nm (B-set) and 300 nm (C-set).

3.5.2. Plastic deformation of TiN100, TiN110 and TiN111

For the plastic deformation study, two sets of eight pillars with square cross-section and aspect ratios of 3 were prepared on each sample (TiN100, TiN110 and TiN111) to investigate the orientational dependency of the plastic deformation in case of TiN. The first set was fabricated with pillar widths of 1 µm (A-set) and the second one with 300 nm (C-Set).

3.6. In-situ pillar compression tests

In-situ pillar compression tests of TiN100 were carried out using a Hysitron PI88 SEM picoindenter in high temperature configuration within a Thermo Scientific Scios 2 DualBeam (SEM-FIB) workstation. Figure 13a shows the individual parts of the Hysitron PI88 SEM picoindenter including the stage, indenter tip, power cable for the heating element, SEM-stage connection,

sample-stage connection, water cooling system, indenter tip heater and the sample heater. Figure 13b reveals the experimental setup within the SEM.

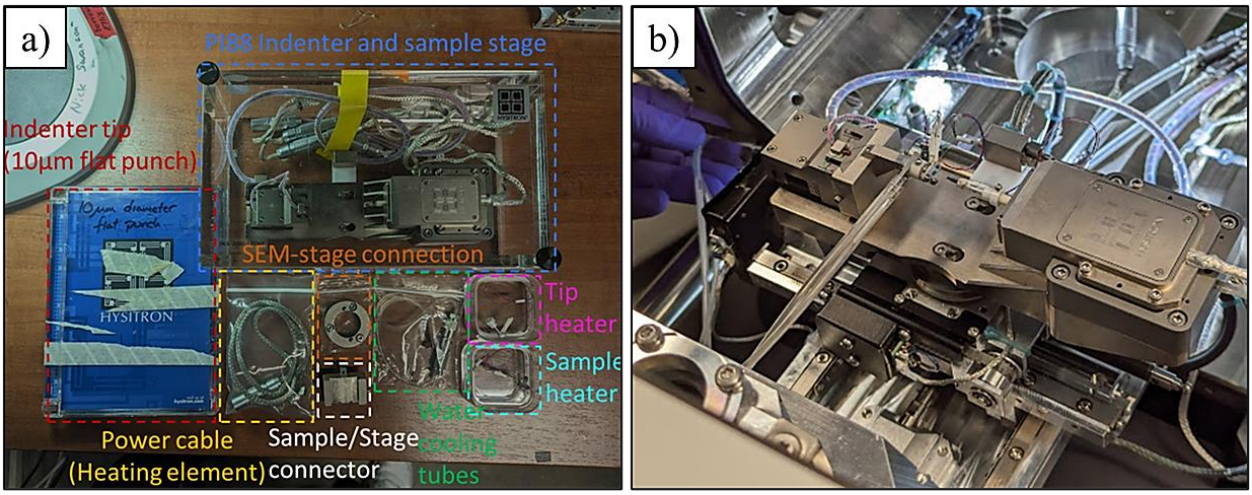

Figure 13: Hysitron PI88 SEM picoindenter outside (a) and inside the SEM (b).

3.6.1. Pillar geometry study in case of TiN100

The pillar geometry study of TiN100 was carried out at 700°C and the sample was fixed on the PI88 stage using a custom-made clamp holder. The tests were performed in displacement-controlled mode using a 10 µm flat punch at a constant strain rate of 6.67×10^{-3} s^{-1}.

3.6.2. Plastic deformation of TiN100, TiN110 and TiN111

Further in-situ pillar compression tests of TiN100, TiN110 and TiN111 could not be carried out due to the failure of the sample heater (figure 14a). The newly purchased heater shown in figure 14b revealed a different geometry and thus a new sample holder had to be manufactured. Furthermore, due to the larger size of the new sample heater compared to the broken one, the samples were too large to be mounted without hitting the intender tip even at maximized working distance (figure 14c). Therefore, the connector part will be shortened in near future to be able to test the samples.

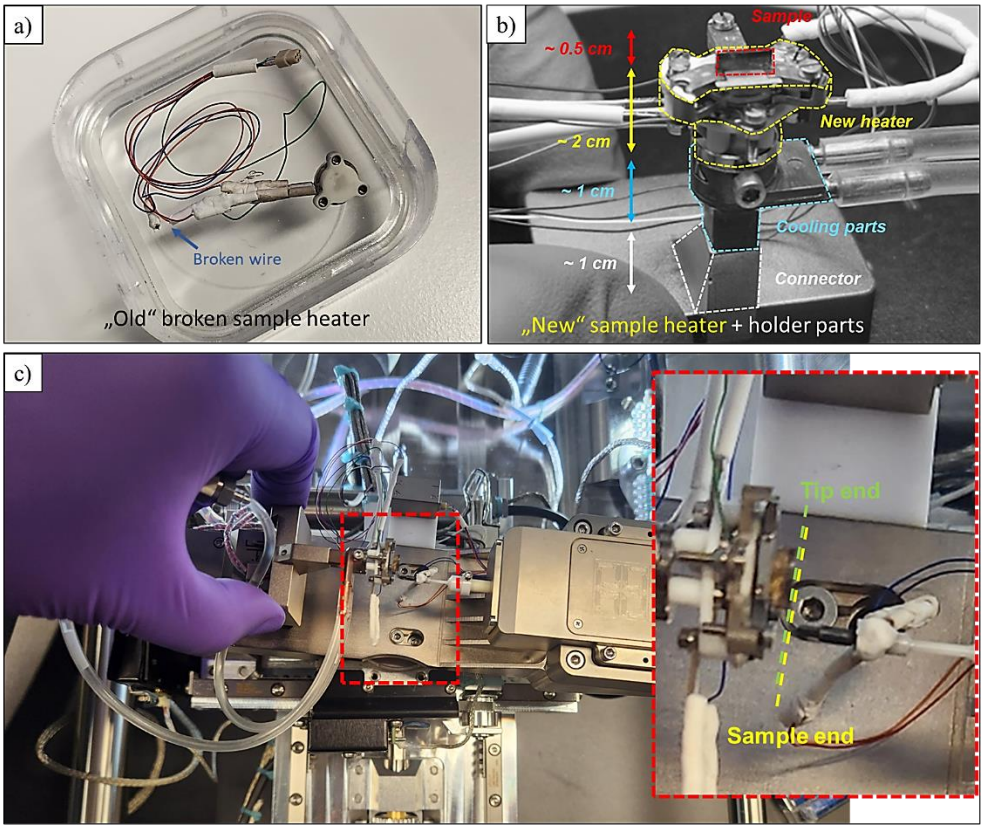

Figure 14: a) Broken sample heater which was used for the parameter study, b) new sample heater with holder parts, c) PI88 configurated with the new sample heater showing that the sample cannot be mounted onto the PI88 stage.

4. Results and discussion

4.1. Chemical vapor deposition

Figure 15 shows an exemplary sample of the first (figure 15a) and the second batch (figure 15b) after CVD of TiN onto the Al_2O_3 substrate. The first sample batch shows insufficient adhesion of the TiN layer compared to the second batch. In general, CVD deposition results in high adhesion forces due to interdiffusion of atoms and thus formation of a strong interface. The insufficient adhesion of the layers of the first sample batch could be either based on poor surface condition of the substrate (cleanliness, roughness etc.) or on unsuitable deposition parameters [37]. All substrates for both batches were polished and cleaned before deposition. In case of the first batch, all ten samples revealed insufficient adhesion whereas the adhesion of the second batch was sufficient. Therefore, it is unlikely that the surface condition of the substrates is the reason for the poor bonding. All deposition parameters were the same for both sample batches except of the deposition pressure and time. The deposition of the first batch was carried out at higher chamber pressure as well as for a longer deposition time. A higher chamber pressure increases the probability of atomic scattering processes and thus gas reactions or etching effects resulting in poor adhesion [38]. Higher deposition times and thus layer thicknesses might increase the residual stresses and result in layer fraction or delamination [39]. In conclusion, the poor layer adhesion of the first sample batch is most likely caused by unsuitable process parameters and can be resolved by a parameter study. Nevertheless, additional characterization would be necessary to determine the exact origin of the poor layer adhesion which would have exceeded the scope of this work. Regarding the further experiments, only the second sample batch was investigated.

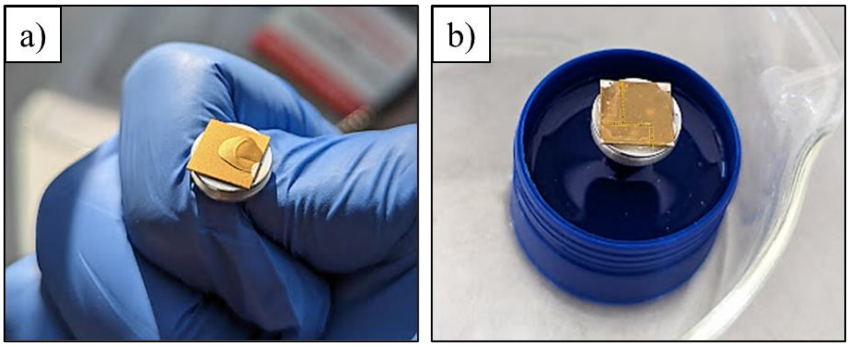

Figure 15: (110) TiN layer epitaxially deposited onto a Al_2O_3 substrate by CVD: a) First sample batch showing insufficient adhesion and b) second sample batch showing sufficient adhesion.

4.2. Femtosecond-laser ablation

Figure 16a shows exemplary the TiN100 sample after fabrication by fs-laser ablation. The sample reveals a well-defined shape without severe cracking during processing which is also observed for the other samples (TiN110 and TiN111). A change in the experimental setup (as described in section 3.6.2) made it necessary to reduce the size of the samples to be able to mount the sample onto the Hysitron PI88 SEM picoindenter stage (figure 16b). During fs-laser ablation, the TiN100 sample with already prepared pillars severely cracked and in-situ pillar compression tests could not be carried out. Wang *et. al.* [40] reported that cracks form at the surface of Al_2O_3 substrates during fs-laser ablation due to thermal stresses and limited plasticity. It is assumed that cracks also formed at the surface of the Al_2O_3 substrate during processing of the TiN100 sample. Due to the small sample dimensions, the cracks might propagate from one sample edge to the other and the sample severly cracked. Instead of cutting the samples, the sample holder will now be cut to be able to carry out in-situ pillar testing without damaging further samples. A new TiN100 sample will be fabricated in Leoben and tested in Berkeley in the near future.

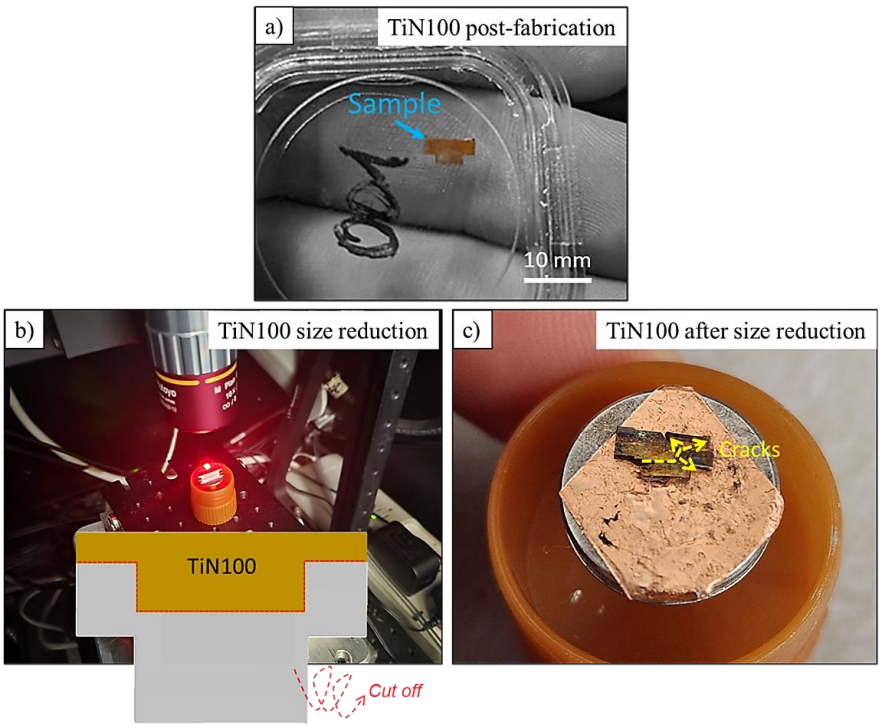

Figure 16: a) T-shaped TiN100 sample exemplary shown after cutting by fs-laser ablation, b) Further size reduction of the TiN100 sample with already prepared pillars on the (100) face and c) cracked sample after processing.

4.3. Electron backscatter diffraction

IPF maps of the TiN100, TiN110 and TiN111 samples were determined by EBSD and are depicted in figure 17. As exemplary shown for TiN100 in figure 17a, the surface of the TiN layer is (110) orientated onto the $(10\bar{1}0)$ Al_2O_3 substrate and has also a distinctive in-plane orientation. Figure 17b reveals the IPF map of the (100) orientated face of the TiN100 sample and the black arrow in the center indicates the indented pillar axis (also valid for TiN110 and TiN111). Figure 17c depicts the IPF map of the (110) face of TiN110 and Figure 17d of the (111) face of TiN111. The results in figure 17 verify that the indented pillar axes of the TiN100, TiN110 and TiN111 samples reveal the desired (100), (110) and (111) orientation, respectively.

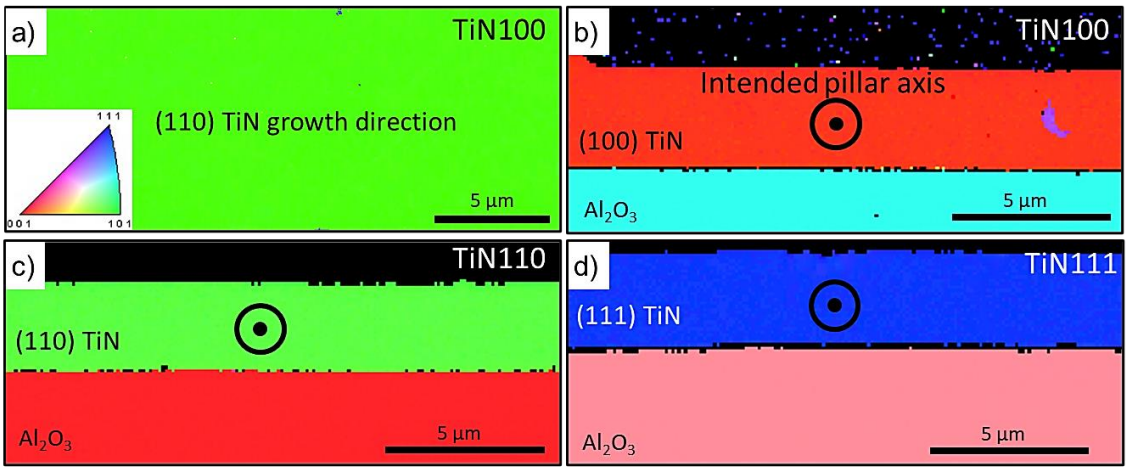

Figure 17: EBSD images of the three TiN samples: a) (110) Growth direction of the layer shown for the TiN100 sample, b) (100) face of the TiN100 sample, c) (110) face of the TiN110 sample and d) (111) face of the TiN111 sample. The black arrow in the center indicates the indented pillar axes.

4.4. Pillar fabrication

4.4.1. Pillar geometry study in case of TiN100

In figure 18, SEM images of the final pillars for the pillar geometry study of TiN100 are depicted. Figure 18a, b and c, show exemplary pillars with a width of 1 µm, 600 nm and 300 nm, respectively. AIII, BIII and CIII at the bottom left of each SEM image are the pillar identifications. Each pillar has a square cross-section and the desired constant aspect ratio of 3. Figure 18d

exemplary reveals the AI pillar after detaching the sample from the SEM sample stamp showing severe contamination. For the sample mounting a silver paint cement was used which seems to migrate into the trenches and contaminating the pillars. For further fabrication of pillars, a conductive copper SEM tape was used instead of the silver paint cement.

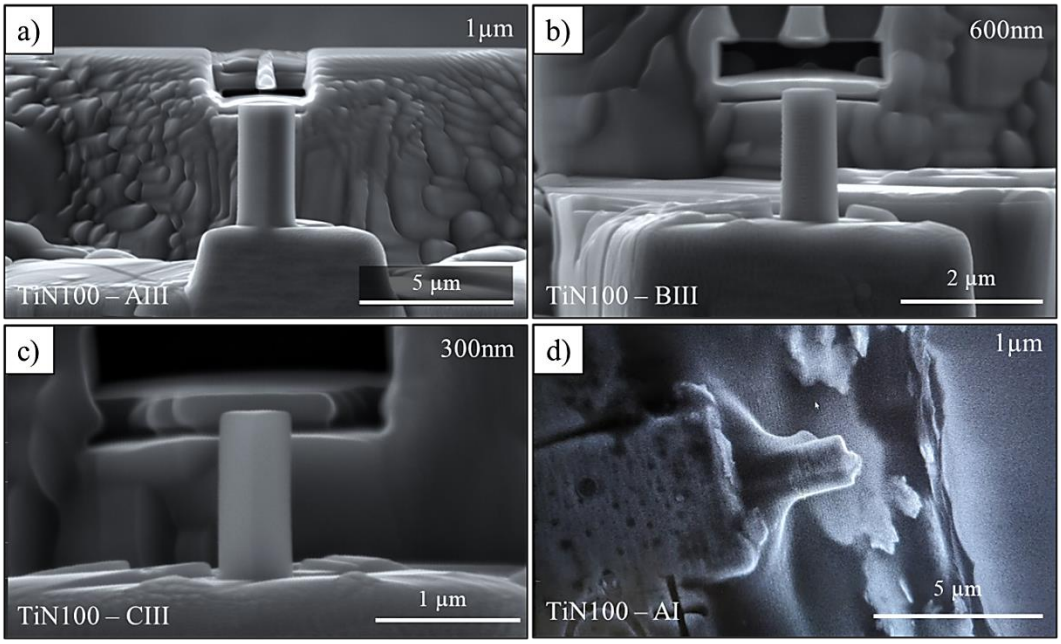

Figure 18: Exemplary pillars of the TiN100 parameter study: Pillar with a) 1 x 1 µm², b) 600 x 600 nm² and c) 300 x 300 nm² cross section, measurement of the d) cross section and e) length of the pillars, f) with silver contaminated pillar after removing the sample of the SEM stamp.

Table 2 represents the list of the 9 fabricated pillars (AI-AIII, BI-BIII, CI-III) for the pillar geometry study of TiN100. AI-AIII are the pillars with an edge width of 1 µm, BI-BIII with 600 nm and CI-CIII with 300 nm. The edge widths S_1, S_2, S_3 and S_4 were used to calculate the area A of the respective pillar after equation (*1*). Furthermore, the average edge width and the pillar length L_0 was used to calculate the aspect ratio AR. Red shaded pillars show severe contamination due to the silver paint cement as explained above and thus these pillars are not further investigated. Pillar FVIII failed during fabrication due to sample drift which is often caused by external or internal mechanical vibrations (e.g., stage drift) [41]. For the pillar geometry study, only FIII and FVI could be investigated by means of in-situ pillar compression tests.

Table 2: Pillar list pointing out the geometries of the TiN100 pillars for the geometry study. The A-set of pillars reveal a pillar edge width of 1 µm, the B-Set of 600 nm and the C-set of 300 nm. S_1, S_2, S_3 and S_4 are the edge lengths of the cross section, L_0 is the length of the pillar, AR is the aspect ratio and A is the area of the cross section.

Pillar	S_1 [nm]	S_2 [nm]	S_3 [nm]	S_4 [nm]	A [µm²]	L_0 [nm]	AR [-]
AI	1104	1160	1174	1079	1,27	3318	2,93
AII	1112	1178	1185	1190	1,36	3350	2,87
AIII	1151	1168	1212	1187	1,39	3308	2,81
BI	567	486	562	488	0,28	1516	2,88
BII	650	594,5	616	650	0,39	1581	2,52
BIII	656	635	696	695	0,45	2054	3,06
CI	391	379	389	417	0,16	1060	2,69
CII	337	268	349	290	0,1	919	2,96
CIII	353	380	386	408	0,15	1140	2,99

4.4.2. Plastic deformation of TiN100, TiN110 and TiN111

Figure 19 depicts SEM images of pillars for TiN100, TiN110 and TiN111 to investigate the plastic deformation and the orientational dependency at elevated temperatures. In figure 19a, b and c, four pillars with 1 µm and four with 300 nm edge width are shown for TiN100, TiN110 and TiN111, respectively. In case of TiN111 (figure 19c), the CVI pillar failed due to mechanical drift as also described for the pillar geometry study in section 4.4.1. Furthermore, exemplary TiN100 pillars with an edge width of 1 µm (figure 19d) and 300 nm (figure 19e) are shown. Both pillars reveal a square cross-section and a constant aspect ratio of 3.

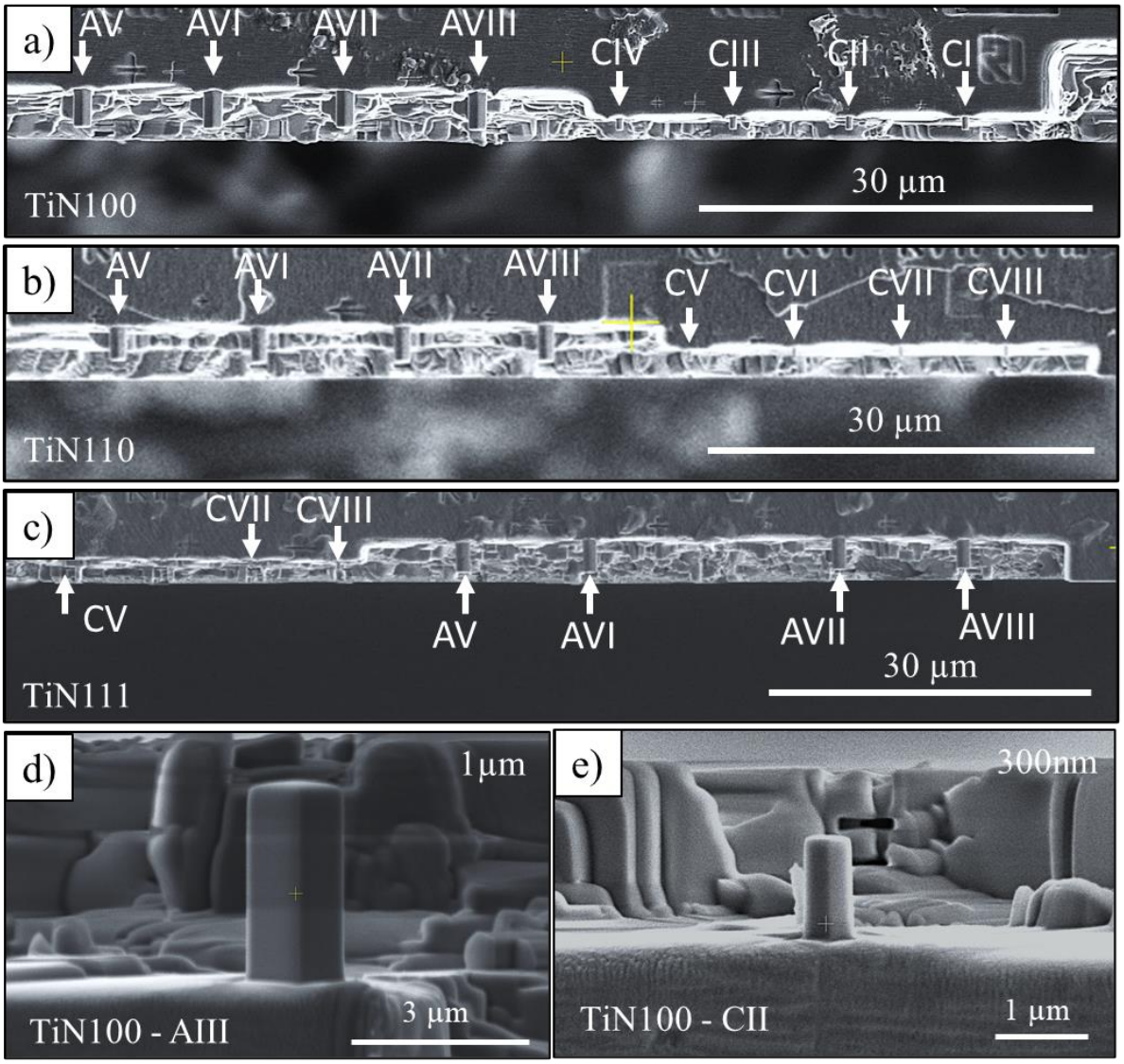

Figure 19: Pillars (4 x 1 µm and 4 x 300 nm) of a) TiN100, b) TiN110 and c) TiN111 indicated by white arrows. Exemplary TiN100 pillars with d) 1µm and e) 300 nm width.

Table 3 represents the exemplary list of the two sets of pillars (A and B-set) for TiN100 to investigate the plastic deformation at elevated temperatures. For TiN110 and TiN111, the equivalent lists can be found in the appendix section 7. AI-AVIII are the pillars with an edge width of 1 µm, CI-CVIII with 300 nm. The edge widths S_1, S_2, S_3 and S_4 were used to calculate the area A of the respective pillar after equation (*1*). Furthermore, the average edge width and the pillar length L_0 was used to calculate the aspect ratio AR. No pillar failed due to mechanical drift in case of TiN100 and TiN110, two failed during preparation of TiN111 (AV and CVI). Nevertheless, the

TiN100 sample severely cracked during size reduction using the fs-laser ablation system as mentioned in sections 3.6.2 and 4.2. The pillars of TiN110 and TiN111 can still be tested which will be carried out in near future at the University of California, Berkeley.

Table 3: Pillar list of TiN100 pointing out the geometries of the pillars for the in-situ pillar compression tests to investigate the plastic deformation at elevated temperatures. The A-set of pillars reveals a pillar width of 1 µm and the C-set of 300 nm. S_1, S_2, S_3 and S_4 are the edge lengths of the cross section, L_0 is the length of the pillar, AR is the aspect ratio and A is the area of the cross section.

Pillar	**S_1 [nm]**	**S_2 [nm]**	**S_3 [nm]**	**S_4 [nm]**	**A [µm²]**	**L_0 [nm]**	**AR [-]**
AI	1000	959	1030	1110	1,05	3320	3,24
AII	929	1210	1200	1020	1,19	3370	3,09
AIII	1010	1150	1170	1080	1,22	3340	3,03
AVII	875	926	1020	964	0,9	3070	3,24
AV	942	901	1030	1040	0,96	2970	3,04
AVI	867	942	1050	1060	0,96	2910	2,97
AVII	949	927	1080	1050	1	3020	3,02
AVIII	894	887	1040	990	0,91	3050	3,20
CI	290	359	384	303	0,11	1130	3,38
CII	309	356	371	342	0,12	1140	3,31
CIII	310	414	391	340	0,13	1140	3,13
CIV	316	373	391	341	0,13	947	2,67
CV	342	366	374	392	0,14	1040	2,82
CVI	326	350	374	343	0,12	1020	2,93
CVII	319	364	410	388	0,14	1040	2,81
CVIII	319	345	360	362	0,12	965	2,78

4.5. In-situ pillar compression tests

4.5.1. Pillar geometry study in case of TiN100

Figure 20 shows the results of the in-situ pillar compression tests at 700 °C for the TiN100 pillar geometry study. As mentioned in section 4.4.1, only two valid tests have been carried out due to the contamination of the residual pillars by the silver paint cement. Figure 20a reveals the stress-strain curves of the AIII pillar with 1 µm and the BIII pillar with 300 nm edge width. Figure 20b and c show the corresponding in-situ SEM images of the AIII and BIII pillar tests, respectively. The BIII pillar reveals higher strength and enhanced crystal plasticity than the one with 1 µm width. This so-called external size effect was reported in many former works for various kinds of micromechanical experiments and materials [34,42,43]. Furthermore, load drops are visible in both stress-strain curves. In general, load drops in displacement-controlled experiments are associated with activation and emission of dislocation sources and following strain generation. The velocity of the induced strain by the dislocation movement is higher than the strain rate of the experiment and thus load drops occur. The pillar is reloaded in an almost elastic manner when the flat punch catches up [30]. In case of the 1 µm pillar, the load drops (I), (II), (III) and (IV) are as high as 100-200 MPa which is about 10-20% of the actual stress. These are rather small load drops and might be minor slip events of individual dislocation groups running out of the pillar surface. The load drop (V) of the BIII pillar however, is as high as 2400 MPa and ends at almost 0 MPa. It is assumed that this load drop is associated with a major slip event of the pillar. The origin of the linear increase in the stress-strain curve starting at 3000 MPa remains unclear. It might be caused by surrounding material (e.g., the silver paint cement) impeding the indenter or pillar movement but should be however, further investigated with more datasets for comparability. There might be another load drop at 5200 MPa but immediately after the beginning, the pillar entirely sheared and no high-resolution images could be obtained. Figure 20d depicts the resolved shear stress (RSS) acting on the individual slip systems for the maximal stresses σ before the load drops (I), (II), (III), (IV) and (V). Furthermore, the calculated Peierl stresses [12] for edge and screw dislocations of the ⟨110⟩{110} and ⟨110⟩{111} slip system are shaded within the graph. The Peierl stresses of the ⟨110⟩{100} are rather high compared to the other slip systems and hence are not displayed in the graph. Taking Schmid's law into account, slip occurs most likely for the ⟨110⟩{110} slip system. For the 1 µm pillar, slip before the load drops (I), (II), (III) and (IV) might occurred by screw dislocation movement. The maximal stress before the load drop (V) of the BIII pillar is almost as

high as the required Peierl stress for edge dislocation movement. It has to be emphasized that the Peierl stress is the required stress for dislocation movement at 0 K. In general, the critical stress for dislocation movement decreases with increasing temperature [44,45]. Taking this into consideration, there might be either ⟨110⟩{110} slip of edge dislocations, screw dislocations or a combination of both during the load drop (V). Furthermore, different slip systems react differently to temperature increases and thus the ⟨110⟩{111} (or even the ⟨110⟩{111}) slip system might be also responsible for high temperature deformations [44]. There are no literature values for critical resolved shear stresses of uniaxial testing at 700 K to the best of our knowledge. Therefore, further experiments will be carried out in near future at the University of California, Berkeley to determine the critical resolved shear stresses and to investigate the deformation mechanisms at elevated temperatures.

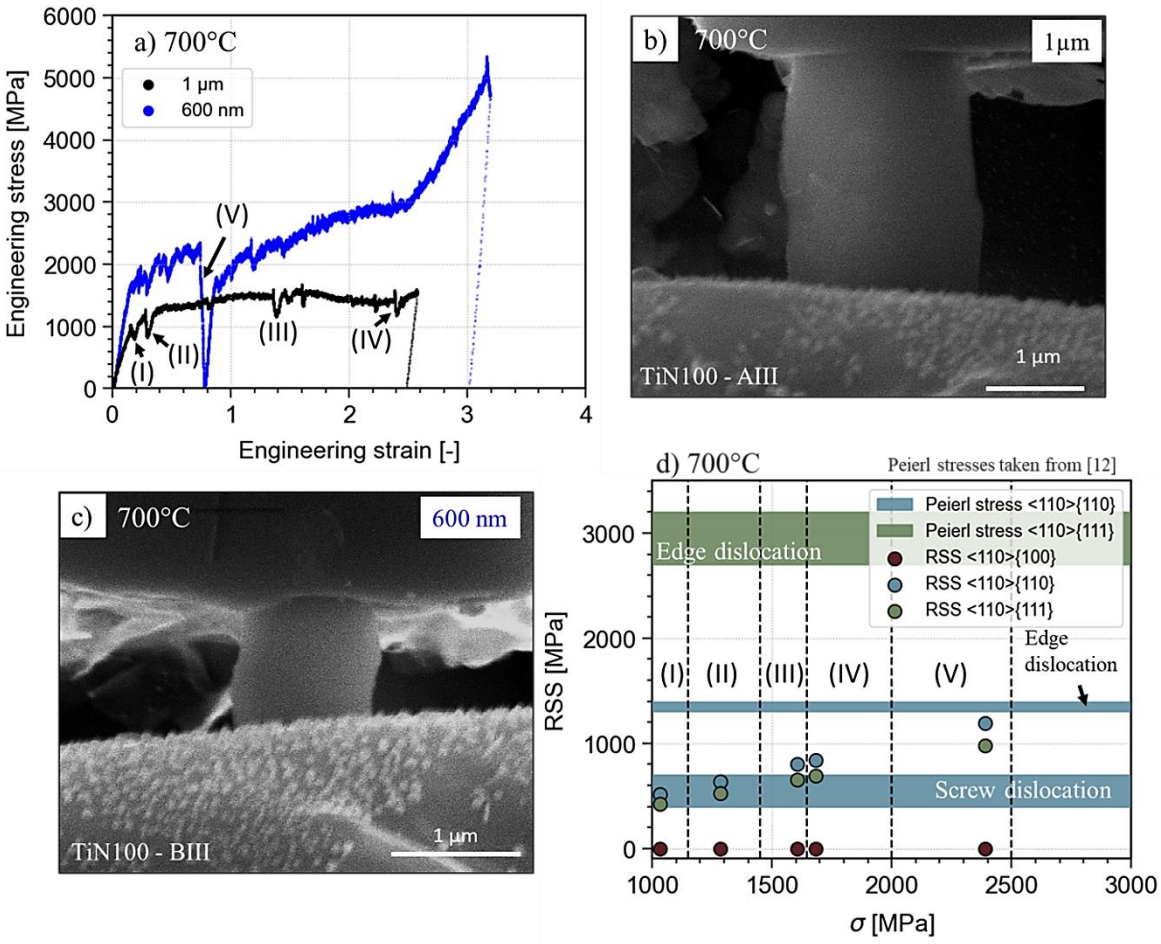

Figure 20: Results of the pillar geometry study showing a) stress-strain curves of the pillar with 1 µm and with 600 nm edge widths, b) SEM image of the 1 µm test and the c) 600 nm test and d) resolved shear stresses of the associated compression stresses acting on the individual slip planes.

4.5.2. Plastic deformation of TiN100, TiN110 and TiN111

As explained in section 3.5.2, no further in-situ pillar compression tests could be carried out due to the failure of the sample heater. The newly purchased sample heater has a different geometry and hence it was not possible to mount the sample without hitting the indenter tip. Nevertheless, due to the promising results of the TiN100 pillar geometry study in figure 20, more in-situ pillar compression tests will be carried out at the University of California, Berkeley. To be able to test the already fabricated samples, the sample/stage connector part will be modified.

5. Conclusions and outlook

The focus of this work was the sample preparation and the investigation the plastic deformation of CVD deposited single crystalline TiN orientated along the three main crystallographic orientation [100], [110] and [111]. Two batches of TiN thin films were deposited onto Al_2O_3 and one batch was further processed by fs-laser ablation. The processed samples were then examined by EBSD and used to prepare pillars for in-situ pillar compression tests using the FIB. First in-situ pillar compression tests of the TiN100 were carried out at 700 °C. The following conclusions can be drawn:

- CVD at 920 °C and 800 mbar for 16 h results in poor layer adhesion (first sample batch). Decreasing the deposition pressure to 160 mbar and the time to 11 h lead to sufficient surface adhesion (second sample batch)
- Fs-laser ablation result in formation of cracks and can cause severe failure if the sample dimensions get too small.
- EBSD showed that the cutting angles of the fs-laser ablation lead to the desired crystallographic orientation along [100], [110] and [111].
- FIB preparation using the introduced 45° cutting approach result in well-shaped pillars with square cross-section down to 300 nm pillar width.
- In-situ pillar compression tests at 700 °C of TiN100 showed higher strength and crystal plasticity for smaller pillar widths and load drops which might be associated to plastic deformation.

The shown results are promising that single crystalline TiN shows plastic deformation at elevated temperatures. As discussed in the previous sections, further in-situ pillar compression tests will be carried out to investigate this topic at the University of Berkeley, California. Prior to testing, the stage-sample connector has to be shortened which will be carried out in the next weeks. Collaborations between the Department of Materials Science Leoben and the Department of Nuclear Engineering Berkeley will be continued in the near future.

6. References

[1] C. Mitterer, PVD and CVD Hard Coatings, Comprehensive Hard Materials (2014) 449–467. https://doi.org/10.1016/B978-0-08-096527-7.00035-0.

[2] W. Schintlmeister, O. Pacher, Preparation and properties of hard-material layers for metal machining and jewelry, Journal of Vacuum Science and Technology 12 (1975) 743–748. https://doi.org/10.1116/1.568659.

[3] M.-A. Nicolet, M. Bartur, Diffusion barriers in layered contact structures, Journal of Vacuum Science and Technology 19 (1981) 786–793. https://doi.org/10.1116/1.571149.

[4] H.O. Pierson, Handbook of refractory carbides and nitrides: Properties, characteristics, processing, and applications, Noyes Publications, Park Ridge, N.J., 1996.

[5] S.M. Borah, H. Bailung, J. Chutia, Decorative Titanium Nitride Colored Coatings on Bell-Metal by Reactive Cylindrical Magnetron Sputtering, Progress in Color, Colorants and Coatings 3 (2010). https://doi.org/10.30509/pccc.2011.75767.

[6] F. Giuliani, C. Ciurea, V. Bhakhri, M. Werchota, L.J. Vandeperre, P.H. Mayrhofer, Deformation behaviour of TiN and Ti–Al–N coatings at 295 to 573 K, Thin Solid Films 688 (2019) 137363. https://doi.org/10.1016/j.tsf.2019.06.013.

[7] G. Dehm, B.N. Jaya, R. Raghavan, C. Kirchlechner, Overview on micro- and nanomechanical testing: New insights in interface plasticity and fracture at small length scales, Acta Materialia 142 (2018) 248–282. https://doi.org/10.1016/j.actamat.2017.06.019.

[8] J.-Å. Schweitz, Mechanical Characterization of Thin Films by Micromechanical Techniques, MRS Bull. 17 (1992) 34–45. https://doi.org/10.1557/S0883769400041646.

[9] J. Buchinger, L. Löfler, J. Ast, A. Wagner, Z. Chen, J. Michler, Z.L. Zhang, P.H. Mayrhofer, D. Holec, M. Bartosik, Fracture properties of thin film TiN at elevated temperatures, Materials & Design 194 (2020) 108885. https://doi.org/10.1016/j.matdes.2020.108885.

[10] J. Li, S. Yang, L. Dong, J. Zhang, Z. Zheng, J. Liu, Effect of crystal orientation on the nanoindentation deformation behavior of TiN coating based on molecular dynamics, Surface and Coatings Technology 467 (2023) 129721. https://doi.org/10.1016/j.surfcoat.2023.129721.

[11] N. Li, S.K. Yadav, X.-Y. Liu, J. Wang, R.G. Hoagland, N. Mara, A. Misra, Quantification of dislocation nucleation stress in TiN through high-resolution in situ indentation experiments and first principles calculations, Sci. Rep. 5 (2015) 15813. https://doi.org/10.1038/srep15813.

[12] S.K. Yadav, R. Ramprasad, A. Misra, X.-Y. Liu, Core structure and Peierls stress of edge and screw dislocations in TiN: A density functional theory study, Acta Materialia 74 (2014) 268–277. https://doi.org/10.1016/j.actamat.2014.04.047.

[13] Space Groups for Solid State Scientists, Academic Pr, 2016.

[14] M.-A. Nicolet, M. Bartur, Diffusion barriers in layered contact structures, Journal of Vacuum Science and Technology 19 (1981) 786–793. https://doi.org/10.1116/1.571149.

[15] S. Massl, W. Thomma, J. Keckes, R. Pippan, Investigation of fracture properties of magnetron-sputtered TiN films by means of a FIB-based cantilever bending technique, Acta Materialia 57 (2009) 1768–1776. https://doi.org/10.1016/j.actamat.2008.12.018.

[16] O. Zaytseva, G. Neumann, Carbon nanomaterials: production, impact on plant development, agricultural and environmental applications, Chem. Biol. Technol. Agric. 3 (2016). https://doi.org/10.1186/s40538-016-0070-8.

[17] K. Choy, Chemical vapour deposition of coatings, Progress in Materials Science 48 (2003) 57–170. https://doi.org/10.1016/S0079-6425(01)00009-3.

[18] D. Zhang, L. Guan, Laser Ablation, in: Comprehensive Materials Processing, Elsevier, 2014, pp. 125–169.

[19] W. Koechner, Solid-State Laser Engineering, sixthth ed., Springer New York; Springer e-books, New York, NY, 2006.

[20] ST Instruments, Ion Milling. https://www.stinstruments.com/samplepreparation/ion-milling/ (accessed accesed on 27 July 2023).

[21] S.A. Campbell, The science and engineering of microelectronic fabrication, (No Title).

[22] M. Malenica, M. Vukomanović, M. Kurtjak, V. Masciotti, S. Dal Zilio, S. Greco, M. Lazzarino, V. Krušić, M. Perčić, I. Jelovica Badovinac, K. Wechtersbach, I. Vidović, V. Baričević, S. Valić, P. Lučin, N. Kojc, K. Grabušić, Perspectives of Microscopy Methods for

Morphology Characterisation of Extracellular Vesicles from Human Biofluids, Biomedicines 9 (2021). https://doi.org/10.3390/biomedicines9060603.

[23] W. Zhou, R. Apkarian, Z.L. Wang, D. Joy, Fundamentals of Scanning Electron Microscopy (SEM), in: W. Zhou, Z.L. Wang (Eds.), Scanning Microscopy for Nanotechnology: Techniques and Applications, Scholars Portal, New York, NY, 2006, pp. 1–40.

[24] A.J. Wilkinson, T.B. Britton, Strains, planes, and EBSD in materials science, Materials Today 15 (2012) 366–376. https://doi.org/10.1016/S1369-7021(12)70163-3.

[25] A.J. Schwartz, M. Kumar, B.L. Adams (Eds.), Electron Backscatter Diffraction in Materials Science, 2nd ed., Springer US, Boston, MA, 2009.

[26] R.A. Schwarzer, D.P. Field, B.L. Adams, M. Kumar, A.J. Schwartz, Present State of Electron Backscatter Diffraction and Prospective Developments, in: A.J. Schwartz, M. Kumar, B.L. Adams (Eds.), Electron Backscatter Diffraction in Materials Science, secondnd ed., Springer US, Boston, MA, 2009, pp. 1–20.

[27] I. Dinaharan, S. Saravanakumar, K. Kalaiselvan, S. Gopalakrishnan, Microstructure and sliding wear characterization of Cu/TiB 2 copper matrix composites fabricated via friction stir processing, Journal of Asian Ceramic Societies 5 (2017) 295–303. https://doi.org/10.1016/j.jascer.2017.06.002.

[28] N. Yao, Focused Ion Beam System—a Multifunctional Tool for Nanotechnology, in: N. Yao, Z.L. Wang (Eds.), Handbook of Microscopy for Nanotechnology, Scholars Portal, Boston, 2005, pp. 247–286.

[29] I. Utke, P. Hoffmann, J. Melngailis, Gas-assisted focused electron beam and ion beam processing and fabrication, Journal of Vacuum Science & Technology B: Microelectronics and Nanometer Structures Processing, Measurement, and Phenomena 26 (2008) 1197–1276. https://doi.org/10.1116/1.2955728.

[30] D. Kiener, C. Motz, G. Dehm, R. Pippan, Overview on established and novel FIB based miniaturized mechanical testing using in-situ SEM, International Journal of Materials Research 100 (2009) 1074–1087. https://doi.org/10.3139/146.110149.

[31] S. Wurster, R. Treml, R. Fritz, M.W. Kapp, E. Langs, M. Alfreider, C. Ruhs, P.J. Imrich, G. Felber, D. Kiener, Novel Methods for the Site Specific Preparation of Micromechanical Structures, Practical Metallography 52 (2015) 131–146. https://doi.org/10.3139/147.110331.

[32] K.J. Hemker, W.N. Sharpe, Microscale Characterization of Mechanical Properties, Annu. Rev. Mater. Res. 37 (2007) 93–126. https://doi.org/10.1146/annurev.matsci.36.062705.134551.

[33] B. Moser, K. Wasmer, L. Barbieri, J. Michler, Strength and fracture of Si micropillars: A new scanning electron microscopy-based micro-compression test, J. Mater. Res. 22 (2007) 1004–1011. https://doi.org/10.1557/jmr.2007.0140.

[34] M.D. Uchic, D.M. Dimiduk, J.N. Florando, W.D. Nix, Sample dimensions influence strength and crystal plasticity, Science 305 (2004) 986–989. https://doi.org/10.1126/science.1098993.

[35] E. Schmid, W. Boas, … Kristallplastizität, Reprint edition, Springer-Verlag; Ingram Content Group, Berlin, Heidelberg, Germany, Lavergne, Tennessee, 2019.

[36] B. Ennis, A review of the effects of chemical and phase segregation on the mechanical behaviour of multi-phase steels, 2016.

[37] G.G. Fuentes, Surface Engineering and Micro-manufacturing, in: Micromanufacturing Engineering and Technology, Elsevier, 2015, pp. 459–486.

[38] S. Sivaram, Chemical Vapor Deposition: Thermal and Plasma Deposition of Electronic Materials, Springer, New York, NY, 2013.

[39] J.G. Kim, J. Yu, A study on the residual stress measurement methods on chemical vapor deposition diamond films, J. Mater. Res. 13 (1998) 3027–3033. https://doi.org/10.1557/JMR.1998.0414.

[40] X.C. Wang, H.Y. Zheng, P.L. Chu, J.L. Tan, K.M. Teh, T. Liu, B.C. Ang, G.H. Tay, High quality femtosecond laser cutting of alumina substrates, Optics and Lasers in Engineering 48 (2010) 657–663. https://doi.org/10.1016/j.optlaseng.2010.02.001.

[41] M.T. Snella, Drift correction for scanning-electron microscopy: Drift correction for scanning-electron microscopy.

[42] S.S. Brenner, Tensile Strength of Whiskers, Journal of Applied Physics 27 (1956) 1484–1491. https://doi.org/10.1063/1.1722294.

[43] A.M. Giwa, Z.H. Aitken, P.K. Liaw, Y.-W. Zhang, J.R. Greer, Effect of temperature on small-scale deformation of individual face-centered-cubic and body-centered-cubic phases of an Al0.7CoCrFeNi high-entropy alloy, Materials & Design 191 (2020) 108611. https://doi.org/10.1016/j.matdes.2020.108611.

[44] Y. Kamimura, K. Edagawa, S. Takeuchi, Experimental evaluation of the Peierls stresses in a variety of crystals and their relation to the crystal structure, Acta Materialia 61 (2013) 294–309. https://doi.org/10.1016/j.actamat.2012.09.059.

[45] G. Gottstein, Physical foundations of materials science, Springer, Berlin, Heidelberg, 2004.

7. Appendix

7.1. TiN110 fabricated pillar list

Table 4: Pillar list of TiN110 pointing out the geometries of the pillars for the in-situ pillar compression tests to investigate the plastic deformation at elevated temperatures. The A-set of pillars reveals a pillar width of 1 µm and the C-set of 300 nm. S_1, S_2, S_3 and S_4 are the edge lengths of the cross section, L_0 is the length of the pillar, AR is the aspect ratio and A is the area of the cross section.

Pillar	S_1 [nm]	S_2 [nm]	S_3 [nm]	S_4 [nm]	A [µm²]	L_0 [nm]	AR [-]
AI	829	835	937	938	0,78	1110	3,20
AII	619	676	811	747	0,51	826	4,28
AIII	800	862	962	960	0,80	1130	3,15
AIV	936	902	954	1000	0,90	1130	3,16
AV	918	881	992	974	0,89	1340	2,96
AVI	821	811	948	895	0,75	1120	3,34
AVII	905	901	982	970	0,88	1210	3,15
AVIII	855	939	957	955	0,86	1190	3,29
CI	356	341	388	381	0,13	541	2,76
CII	343	334	356	375	0,12	468	2,98
CIII	380	322	356	376	0,13	435	2,96
CIV	398	348	395	388	0,15	478	2,72
CV	256	277	292	280	0,08	373	3,08
CVI	237	251	260	245	0,06	302	3,82
CVII	240	278	262	238	0,06	338	3,66
CVIII	227	239	261	241	0,06	359	3,93

7.2. TiN111 fabricated pillar list

Table 5: Pillar list of TiN111 pointing out the geometries of the pillars for the in-situ pillar compression tests to investigate the plastic deformation at elevated temperatures. The A-set of pillars reveals a pillar width of 1 µm and the C-set of 300 nm. S_1, S_2, S_3 and S_4 are the edge lengths of the cross section, L_0 is the length of the pillar, AR is the aspect ratio and A is the area of the cross section.

Pillar	S_1 [nm]	S_2 [nm]	S_3 [nm]	S_4 [nm]	A [µm²]	L_0 [nm]	AR [-]
AI	806	880	966	883	0,78	2970	3,36
AII	606	880	966	816	0,67	3010	3,68
AIII	872	874	938	900	0,80	2930	3,27
AIV	845	884	986	914	0,82	2860	3,15
AV	FAILED						
AVI	879	899	996	931	0,86	3111	3,36
AVII	793	995	1060	931	0,89	3002	3,18
AVIII	762	917	993	879	0,79	2710	3,05
CI	301	359	359	332	0,11	996	2,95
CII	323	337	371	317	0,11	1001	2,97
CIII	286	317	336	345	0,1	958	2,98
CIV	307	295	314	336	0,1	977	3,12
CV	206	201	245	240	0,05	916	4,11
CVI	FAILED						
CVII	183	268	228	233	0,05	861	3,78
CVIII	240	277	325	303	0,08	888	3,1